Journal of Nanobiotechnology

RESEARCH

Open Access

GSH-responsive polymeric micelles-based augmented photoimmunotherapy synergized with PD-1 blockade for eliciting robust antitumor immunity against colon tumor

Chenlu Huang[1,2†], Xinyu Yang[1,2†], Huidong Li[2†], Li Zhang[1,2], Qing Guo[1,2], Qingyu Yu[1,2], Hai Wang[1,2], Linhua Zhang[1,2*] and Dunwan Zhu[1,2*]

Abstract

Phototherapy is a promising antitumor modality, which consists of photothermal therapy (PTT) and photodynamic therapy (PDT). However, the efficacy of phototherapy is dramatically hampered by local hypoxia in tumors, overexpression of indoleamine 2,3-dioxygenase (IDO) and programmed cell death ligand-1 (PD-L1) on tumor cells. To address these issues, self-assembled multifunctional polymeric micelles (RIMNA) were developed to co-deliver photosensitizer indocyanine green (ICG), oxygenator MnO_2, IDO inhibitor NLG919, and toll-like receptor 4 agonist monophosphoryl lipid A (MPLA). It is worth noting that RIMNA polymeric micelles had good stability, uniform morphology, superior biocompatibility, and intensified PTT/PDT effect. What's more, RIMNA-mediated IDO inhibition combined with programmed death receptor-1 (PD-1)/PD-L1 blockade considerably improved immunosuppression and promoted immune activation. RIMNA-based photoimmunotherapy synergized with PD-1 antibody could remarkably inhibit primary tumor proliferation, as well as stimulate the immunity to greatly suppress lung metastasis and distant tumor growth. This study offers an efficient method to reinforce the efficacy of phototherapy and alleviate immunosuppression, thereby bringing clinical benefits to cancer treatment.

Keywords Polymeric micelles, Phototherapy, Immunotherapy, Indoleamine 2,3-dioxygenase (IDO), Immune checkpoint inhibitor, Hypoxic tumor microenvironment

†Chenlu Huang, Xinyu Yang and Huidong Li have authors contributed equally to this work.

*Correspondence:
Linhua Zhang
zhanglinhua@bme.pumc.edu.cn
Dunwan Zhu
zhudunwan@bme.pumc.edu.cn
Full list of author information is available at the end of the article

Graphical Abstract

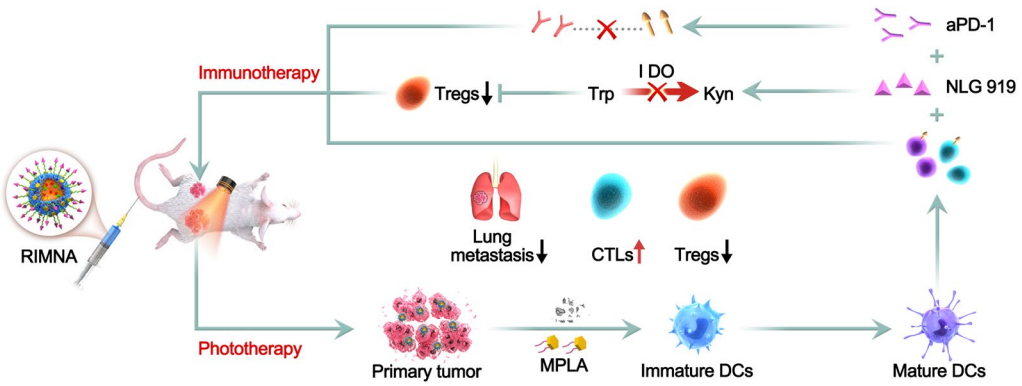

Introduction

Multimodal synergistic therapy that integrates the advantages of single therapy exhibits a remarkable super-sum effect and great prospects for development in tumor treatment [1]. The advent of nanotechnology offers unprecedented foreground for multimodal synergistic therapies, which can consolidate therapeutics with different functions into a single nanosystem to produce significant antitumor efficacy [2–5]. Phototherapy, consisting of photothermal therapy (PTT) and photodynamic therapy (PDT), has become a promising tumor treatment modality due to its strengths of less drug resistance, rapid healing and good efficacy [6]. The combined strategy of PTT and PDT can realize better treatment outcomes with fewer photosensitizer doses, lower irradiation power, and shorter treatment duration, as well as less side effects on normal tissues [7, 8]. PTT-mediated hyperthermia can boost the permeability of cell membranes and enhance the uptake of photosensitizer-loaded nanocarriers by tumor cells as well as improve local blood flow and increase the O_2 concentration in tumor tissues, thus promoting the generation of reactive oxygen species (ROS) [9, 10]. In turn, ROS produced during PDT can destroy heat shock proteins, thereby weakening their protective effect on tumor cells during PTT [11, 12]. As an near-infrared (NIR) fluorescent dye, indocyanine green (ICG) is approved by U.S. Food and Drug Administration (FDA) one and only for in vivo applications and also acts as a photosensitizer [13]. Although ICG-loaded nanocarriers improve some shortcomings of free ICG, such as easy aggregation, low ROS yield, and poor stability [14]. However, its efficacy of PDT is dramatically reduced due to the hypoxic microenvironment in the tumor [15, 16]. To overcome this problem, MnO_2 is introduced to catalyze the formation of O_2 from overexpressed H_2O_2 in the tumor microenvironment (TME), thereby generating sufficient ROS during ICG-mediated PDT to induce apoptosis of tumor cells [17–19]. Phototherapy can effectively inhibit the primary tumor, but it is difficult to restrain the metastasis and recurrence of the tumor [20].

Metastatic tumor that spreads to distant organs accounts for more than 90% of tumor-related deaths [21]. At present, the two biggest challenges in clinical tumor treatment are to prevent the metastasis of local tumor and avoid recurrence [22]. To settle these problems, better treatments must be developed to kill tumor cells extensively and completely. Tumor immunotherapy is a method that can prevent the metastatic spread of local tumor and avoid recurrence by boosting the immune system to identify and kill tumor cells [23]. Although PTT and PDT have been reported to produce tumor-associated antigens (TAAs) and activate acute inflammation to evoke tumor-specific immunity, the efficacy of antitumor immunity is limited [24]. Tumor cells evade the recognition by the immune system due to various immune-negative regulatory signals that inhibit T cell activation, which may be the reason for the failure of antitumor immunotherapy [25]. Therefore, one of the most effective tactics is inhibition of negative immunomodulation to reactivate the antitumor immune response [25–27]. Tumor cells overexpress indoleamine 2,3-dioxygenase (IDO), which is in charge of catalyzing the transition of tryptophan (Trp) to kynurenine (Kyn), subsequently promotes the expansion of immunosuppressive regulatory T cells (Tregs) and inhibits the proliferation and activation of antitumor effector T cells, thus facilitating the immune escape of tumor cells in the TME [28–30]. In addition, programmed cell death ligand-1 (PD-L1) overexpressed on tumor cells binds to programmed death receptor-1 (PD-1) on T cells to induce exhaustion of T cell, which

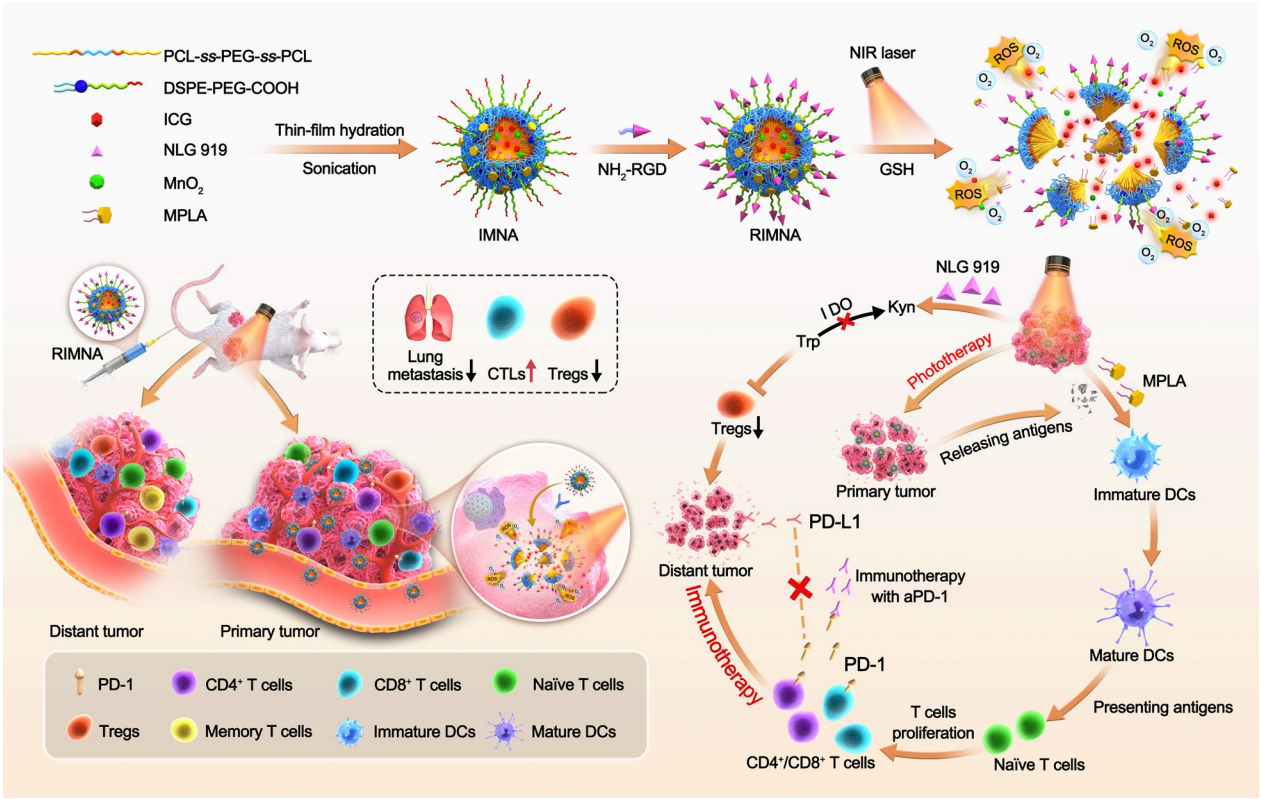

Scheme 1 Schematic illustration of RIMNA polymeric micelles as amplifier for robust photoimmunotherapy synergized with PD-1 blockade antibody against primary tumors, distant tumors, and lung metastasis

also grants tumor cells to avoid immune surveillance [31, 32]. Considering the immune escape pathway, several immune checkpoint inhibitors of IDO and PD-1/PD-L1 have been exploited to reprogram the immunosuppressive microenvironment in preclinical and clinical trials [33]. Nevertheless, phase III clinical trials of IDO inhibitors have failed [34], and the clinical response rate to PD-1/PD-L1 blockade is only 10%~30% [35]. Rational combination therapy strategies have attracted widespread attention by transforming "cold" tumors into "hot" tumors to trigger infiltration of T cell into tumors through various methods (e.g. chemotherapy, radiotherapy, phototherapy, etc.) [36–39].

Herein, we fabricated multifunctional polymeric micelles (Arginylglycylaspartic acid (RGD)-ICG/MnO_2/NLG919/monophosphoryl lipid A (MPLA)@polymeric micelles, labeled as RIMNA) for the synergistic treatment of enhanced PTT-PDT-immunotherapy. RIMNA polymeric micelles loaded with photosensitizer ICG, oxygenator MnO_2 and IDO inhibitor NLG919 were synthesized by thin-film hydration plus sonication method, as well as toll-like receptor (TLR) 4 agonist MPLA were inserted on the surface. As shown in Scheme 1, the treatment strategy was mainly conducted *via* the steps as follows: (1) RIMNA polymeric micelles accumulated into the tumor after systemic administration, then responded to NIR laser and high glutathione (GSH) in TME to release drugs. (2) The excess H_2O_2 in TME provided sufficient substrate for MnO_2 exerting an enzymatic reaction to produce O_2, which could ameliorate the hypoxic status in tumors and promote PDT efficacy. Besides, MnO_2 also enhanced the PTT effect of ICG. (3) Under NIR laser irradiation, RIMNA polymeric micelles killed primary tumors by PDT/PTT synergistic treatment, as well as released TAAs. (4) TAAs and MPLA were absorbed by immature dendritic cells (DCs) and induced DCs maturation, thereby activating antitumor immune responses. (5) Subsequently, the IDO-mediated Trp/Kyn immune escape pathway was blocked by NLG919, which reduced Tregs ratio and strengthened the function of effector T cells. (6) PD-1 blockade antibody further improved tumor-specific immune responses, prevented distant tumors growth and lung metastasis. RIMNA-based photoimmunotherapy in combination with PD-1 blockade antibody offered a promising strategy to fight tumor.

2. Materials and methods

2.1. Preparation of RIMNA

The polymeric micelles RIMNA were prepared using thin-film hydration plus sonication method based on polyethylene polycaprolactone-*ss*-polyethylene glycol-*ss*-polyethylene polycaprolactone (PCL-*ss*-PEG-*ss*-PCL) copolymer synthesized by our research group. First, MnO_2 and hydrophobic ICG were fabricated according to the previous literature [40]. Next, PCL-*ss*-PEG-*ss*-PCL (20 mg), ICG (1 mg), DSPE-PEG-COOH (1 mg), NLG919 (1 mg), MPLA (20 μg) and MnO_2 (0.2 mg) were dissolved in an eggplant bottle with dichloromethane and sonicated for 5 min. Then a thin film was obtained by rotary evaporation to remove dichloromethane and hydrated at 65 °C drying oven for 5 h. Subsequently, the mixture was sonicated using a probe sonicator in ice bath for 10 min and dialyzed with deionized water to remove free drugs. Finally, RIMNA was acquired after NH_2-RGD ligation by 1-(3-Dimethylaminopropyl)-3-ethylcarbodiimide (EDC)/N-Hydroxysuccinimide (NHS) activation reaction. RINA (without MnO_2 loading), RIMA (without NLG919 loading), and RIMN (without MPLA loading) were formulated by the similar methods as depicted above.

Cellular uptake study in vitro

CT26 cells were cultured in confocal plates overnight and fresh roswell park memorial institute (RPMI) 1640 medium containing Free ICG, RINA, and RIMNA (ICG: 10 μg/mL) were added. After co-incubation for 2 h, the cells were irradiated with 808 nm laser (1.5 W/cm^2, 5 min). After incubation for another 2 h, confocal laser scanning microscope (CLSM, Zeiss LSM 710, Jena, Germany) was used to observe the cells after Hoechst staining.

Intracellular ROS generation assay in vitro

Phosphate buffer saline (PBS), RINA, and RIMNA were co-cultured with CT26 cells for 2 h (ICG: 10 μg/mL). Next, the cells were incubated with 2',7'-dichlorodihydrofluorescein diacetate (carboxy-H_2DCFDA) for 15 min at 37 ℃. Then the cells were washed once with PBS and irradiated with 808 nm laser for 5 min (1.5 W/cm^2). Intracellular ROS levels were detected by CLSM and flow cytometry (BD FACS Calibur, USA).

Cytotoxicity assay in vitro

CT26 cells were inoculated into 96-well plates and co-incubated with RIMNA, RINA, and Free ICG (ICG equivalent concentration was 2.5, 5, 10 and 20 μg/mL) for 24 h. In the laser irradiation group, the cells were irradiated with 808 nm laser for 5 min (1.5 W/cm^2). After that, 100 μL RPMI1640 medium mixed with CellTiter 96 Aqueous One Solution Cell Proliferation Assay (MTS) (20 μL of MTS in every 100 μL RPMI1640 medium) was added to each well, and the cells were incubated in the incubator for 30 min followed by being assessed with a Varioskan Flash Multimode Reader (Thermo Fisher Scientific, USA).

IDO inhibition

CT26 cells (1.5×10^4) were seeded into a 24-well plate, and 50 ng/mL of interferon (IFN)-γ was added into each well and incubated overnight to stimulate the IDO expression. After that, the cells were co-cultured with PBS, NLG919, RIMA, RIMNA and RIMNA + Laser (the concentration of NLG919 was 5 μg/mL) for 24 h, respectively. After incubation for 2 h, the cells treated with RIMNA + Laser were irradiated with 808 nm laser (1.5 W/cm^2, 5 min) and co-incubated for another 22 h. After that, the supernatants were collected and the contents of Kyn and Trp were measured with enzyme linked immunosorbent assay (ELISA) kits.

Tumor accumulation study in vivo

CT26 cells (1×10^6) were inoculated into the right buttock of female BALB/c mice (6–8 weeks old) to establish CT26 tumor-bearing mouse model. When the tumors grew to ~200 mm^3, the mice were randomly divided into RIMNA, Free ICG and PBS groups to observe the tumor accumulation of polymeric micelles after intravenous administration (ICG dose: 5 mg/kg, $n=5$). In vivo imaging was performed at 6, 12, 24, 48 and 72 h post injection.

PTT-PDT synergistic antitumor study in vivo

CT26 cells (1×10^6) were injected subcutaneously in the right buttock of BALB/c mice (6–8 weeks old) on day 0. And the mice were divided into 4 groups on day 7: (1) RIMNA + Laser; (2) RINA + Laser; (3) Free ICG + Laser; (4) PBS + Laser (ICG dose: 5 mg/kg), of which the tumors received 808 nm laser (1.5 W/cm^2) for 5 min at 24 h and 48 h after tail vein intravenous administration every 5 days and observed with Fluke infrared imaging device to record the temperature change. Finally, the treated mice were sacrificed to collect the tumor and major organs from all groups for hematoxylin and eosin (H&E) analysis on day 15. And the hypoxia and ROS generation of tumor cells were investigated *via* immunofluorescence staining methods. For the hypoxia study, after intraperitoneal injection of pimonidazole hydrochloride 1.5 h into the mice, the tumors were collected and sliced into sections. The tumor sections were blocked by 10% donkey serum and incubated with hyproxyprobe-1 and FITC-labeled anti-IgG (H + L) second antibody following the manufacturer's instructions. For the ROS level study, the tumors

were irradiated with 808 nm laser (1.5 W/cm^2, 5 min) after dichlorodihydrofluorescein diacetate (DCFH-DA) intratumorally injected into the mice for 2 h. Then the tumor tissues were collected and sliced into sections. All the sections were stained with DAPI before being detected by CLSM.

Abscopal effect study

The tumor-bearing mouse models were established by inoculating CT26 cells (1×10^6) into the right flank of the BALB/c mice on day 0. CT26 cells (2×10^5) were inoculated into the left flank on day 6. Once the volumes of primary tumors reached about 80 mm^3 on day 7, RIMNA, RINA, RIMA, RIMN, I+N+A, and PBS (ICG dose: 5 mg/kg, $n=5$) was intravenously (*i.v.*) injected to the mice, respectively. These treatments were operated twice with an interval of 5 days. At 24 and 48 h after intravenous injection, the primary tumors of the mice were irradiated with 808 nm laser (1.5 W/cm^2, 5 min). 100 μg aPD-1 was injected intraperitoneally every 3 days for 4 times [41]. The tumor volumes and body weights of mice were noted every two days. The tumor volume (V) was calculated by using the equation: V = 0.5 × length × width^2. When the tumor volumes reached 2000 mm^3, the mice were ethically required to be euthanized.

Immune responses study

On day 21, spleens, tumor-draining lymph nodes, and tumors of the treated mice were harvested and prepared into single-cell suspensions. The obtained single cells were co-marked with anti-CD11c, anti-CD80, anti-CD40, and anti-CD86 antibodies for analyzing the mature DCs; co-stained with anti-CD3, anti-CD4, and anti-CD8 antibodies for analyzing the $CD4^+$ and $CD8^+$ T cells; co-marked with anti-CD4, anti-CD8, and anti-CD69 antibodies for analyzing the activation of $CD4^+$ and $CD8^+$ T cells; co-marked with anti-CD4, anti-CD8, and anti-IFN-γ antibodies for analyzing the IFN-γ-secreting T cells; co-marked with anti-CD4 and anti-Foxp3 antibodies for the analysis of the Tregs; and co-marked with anti-CD4, anti-CD8, anti-CD44, and anti-CD62L antibodies to measure the central memory T cells according to the procedures of the manufacturer by using flow cytometry. Meanwhile, the sera were also collected to detect tumor necrosis factor-α (TNF-α) and interleukin-4 (IL-4) through ELISA kits.

Tumor metastasis inhibition

The mice treated as described in part "Abscopal effect study" received tail vein injection of CT26 cells (1×10^5) on day 20. For analyzing metastasis, the lungs were collected and prepared for H&E staining on day 30.

Statistical analysis

All data were displayed as mean ± standard error of mean (SEM). All statistical analyses were presented using GraphPad Prism by one-way or two-way analysis of variance (ANOVA) and $P<0.05$ was considered statistically significant.

Results and discussion

Preparation and characterization

Multifunctional polymeric micelles (RIMNA) with phospholipid layer and drug loaded core were constructed using thin-film hydration plus sonication method to encapsulate photosensitizer ICG, oxygenator MnO_2, IDO inhibitor (NLG919), and TLR4 agonist MPLA. The transmission electron microscopy (TEM) images of RIMNA presented regular spherical shape (Fig. 1A). The average hydrodynamic diameter and zeta potential of RIMNA were 161.87 ± 4.14 nm and −22.3 ± 0.01 mV, respectively. And the particle size of RIMNA was between 160 and 180 nm and kept steady within 7 days, which was able to realize high accumulation into the tumor site *via* enhanced permeability and retention (EPR) effect (Fig. 1B) [42]. Dynamic light scattering (DLS) further showed that RIMNA had a homogeneous distribution with a narrow dispersion in PBS solution (pH 7.4) (Fig. 1C). Besides, we detected the particle size change of RIMNA in GSH solution to verify the reduction sensitivity. The results showed that there were two broad peaks in the presence of GSH, suggesting that *-ss-* was destroyed to cause the fragmentation of RIMNA under reductive condition. The ultraviolet-visible (UV-vis) absorption spectra revealed that the characteristic absorption peak of ICG and NLG919 were at ~780 nm and ~280 nm, respectively, which indicated the successful loading of ICG and NLG919 in RIMNA (Fig. 1D). The photothermal efficiency of RIMNA was also studied in Fig. 1E and F, and the results demonstrated that the temperature rise of RIMNA, RINA, and Free ICG were 53.4 ℃, 50.8 ℃, and 45.8 ℃, respectively. By comparison, PBS solution showed a negligible rising of temperature, indicating that polymeric micelles ameliorated the defect of free ICG and the presence of MnO_2 enhanced the PTT effect [43–45].

Cellular uptake, ROS generation, and cytotoxicity in CT26 tumor cells

As shown in Fig. 1G, polymeric micelles enabled enhanced uptake of ICG by CT26 tumor cells. It's worth mentioning that the cellular uptake of ICG in Free ICG, RINA and RIMNA groups significantly increased when cells exposed to NIR laser irradiation, which may be ascribe to that the temperature elevation enhanced the

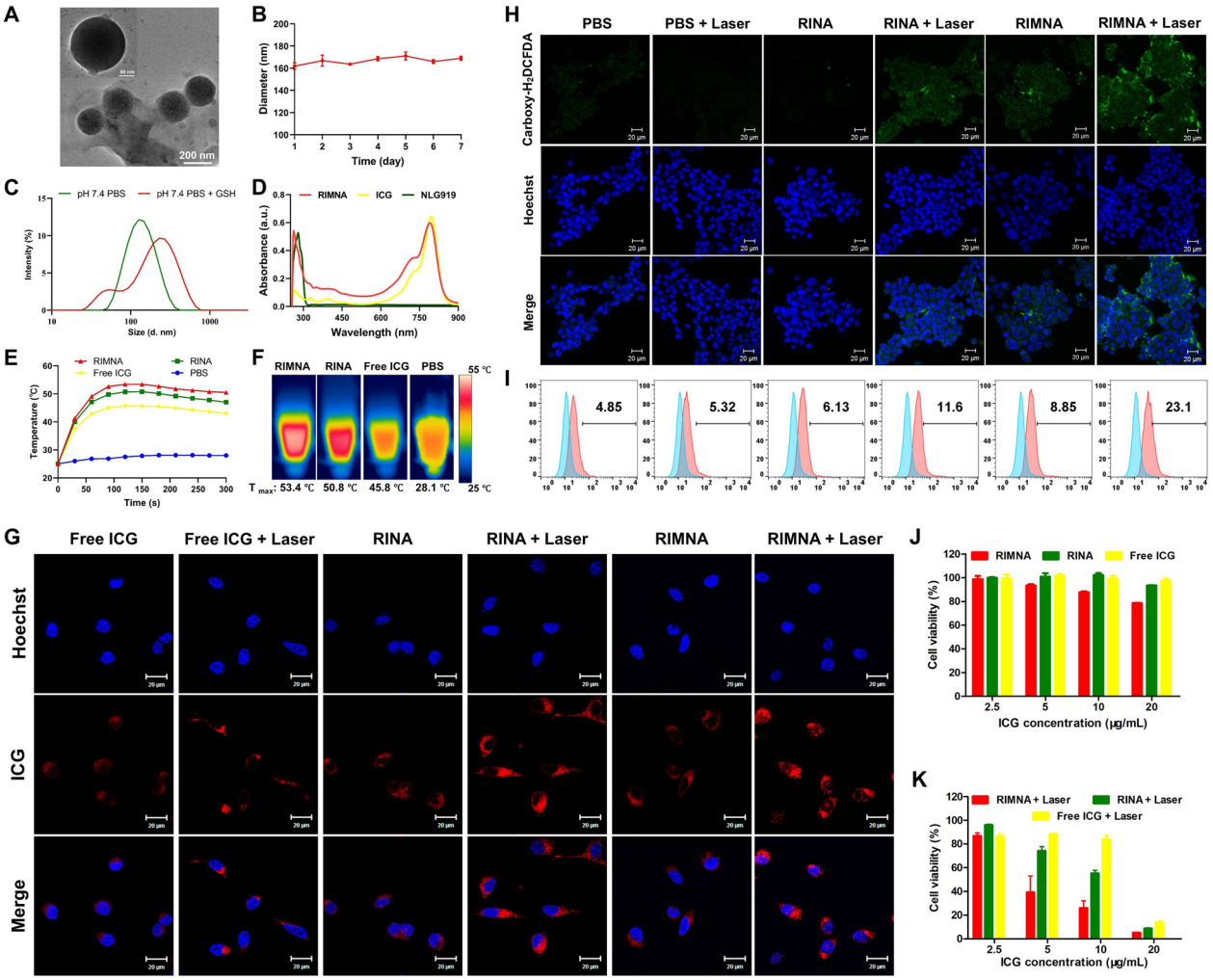

Fig. 1 Characterization and CT26 cell-level evaluation of RIMNA. (**A**) TEM images of RIMNA (Scale bar = 50–200 nm). (**B**) The particle size stability of RIMNA stored at 4 ℃ ($n = 3$). (**C**) The particle size distribution of RIMNA in PBS solution (pH 7.4) with or without GSH. (**D**) The absorption spectra of RIMNA, ICG, and NLG919. (**E**) Temperature curves and (**F**) corresponding infrared thermal imageries of RIMNA, RINA, Free ICG, and PBS under NIR laser irradiation. (**G**) The CLSM images indicated cellular uptake (Scale bar = 20 μm). (H) The CLSM images and (**I**) representative flow cytometric plots indicated ROS production (Scale bar = 20 μm). The survival rate of CT26 cells incubated with various concentrations of RIMNA, RINA or Free ICG (**J**) without or (**K**) with NIR laser irradiation ($n = 3$)

fluidity and permeability of cell membrane [46]. Next, ROS probe carboxy-H_2DCFDA was used to determine the intracellular ROS production. There was almost no ROS produced in the cells dealt with PBS, PBS + Laser or RINA (Fig. 1H). And compared with non-laser irradiation group, the green fluorescence signal of RINA was enhanced after laser irradiation. The cells incubated with RIMNA exhibited weak ROS fluorescence [47], and the intracellular ROS signals dramatically augmented when the laser irradiation was carried out. What's more, the flow cytometry histograms displayed the similar results to the CLSM images, which demonstrated that both laser irradiation and the introduction of MnO_2 improved the level of intracellular ROS (Fig. 1I).

PEG/PCL copolymers approved by the U.S. FDA have been extensively explored as potential drug delivery vehicles, which is non-toxic and biocompatible [48]. As an NIR fluorescent dye, ICG is approved by the U.S. FDA for clinical use [49]. MTS assay was used to evaluate the biocompatibility of polymeric micelles and phototherapy-caused cytotoxicity of RIMNA (Fig. 1J and K). RINA exhibited no damage to CT26 cells, indicating polymeric micelles were biocompatible and safe. The slight cytotoxicity of RIMNA at high concentrations may be the results of MnO_2-mediated Fenton reaction [50]. RIMNA,

RINA, and Free ICG all exhibited concentration-dependent phototoxicity to CT26 cells under laser irradiation. When the concentration of ICG reached 10 μg/mL, the cell survival rate treated with RINA + Laser group was about 50%, while that of RIMNA + Laser group decreased significantly to about 20%. Therefore, RIMNA plus laser irradiation could effectively kill tumor cells through PTT-PDT effects. To detect the inhibitory effect of RIMNA on IDO pathway, CT26 cells were treated with PBS, NLG919, RIMA, RIMNA and RIMNA + Laser, and the contents of Kyn and Trp were measured with ELISA kits. As shown in Fig. S1 (Supporting Information), the ratio of Kyn to Trp treated with NLG919 exhibited an apparent decline. Compared with PBS and RIMA groups, the ratio of Kyn to Trp in RIMNA and RIMNA + Laser treated group decreased greatly, demonstrating the inhibition effect of RIMNA polymeric micelles on IDO signal pathway caused by NLG919.

3.3. Tumor accumulation in vivo

In vivo imaging was proceeded to surveillance the accumulation of polymeric micelles after intravenous administration. CT26 tumor-bearing mice of the three groups (PBS, Free ICG, and RIMNA) were tracked at 6, 12, 24, 48, and 72 h post injection (Supporting Information Fig. S2). For the PBS group, no signal was observed at each time point. The signal of Free ICG was found at 6 h, while negligible signal was observed after 48 h because of the rapid metabolism of ICG. In contrast, the fluorescence of RIMNA was stronger than that of Free ICG at all time points, and the maximum accumulation of ICG at the tumor site was attained after 24 h of intravenous administration, proving that EPR effect based on polymeric micelles could facilitate tumor accumulation [51].

PTT-PDT effect in vivo

The antitumor capacity of RIMNA-based PTT-PDT was estimated through CT26 subcutaneous tumor model and the schematic illustration of the treatment plan was displayed in Fig. 2A. CT26 tumor-bearing mice were irradiated with 808 nm laser (1.5 W/cm^2) at 24 h and 48 h after administration of PBS, Free ICG, RINA, and RIMNA. The PBS group induced the least change in temperature even being irradiated for 5 min (Fig. 2B-D). The Free ICG group showed an ineffective temperature elevation (below 44 °C) due to poor stability, short retention time, high clearance rate, and less tumor accumulation [14]. An enhanced photothermal conversion effect was observed in RINA treatment group, and the temperature of tumor increased to 51.3 °C. Surprisingly, owing to the MnO_2-enhanced PTT effect, the RIMNA group showed a dramatic temperature increase to 54.9 °C, demonstrating its favorable photothermal capacity. Notably, even after 48 h of intravenous injection, the tumor site achieved 54.1 °C under laser irradiation, which illustrated RIMNA enhanced the in vivo stability and intratumoral accumulation of ICG. Furthermore, we investigated hypoxia of tumor tissues *via* immune-fluorescence staining methods. Hyproxyprobe-1 combined with anti-FITC antibody were applied to evaluate the hypoxia status in tumor. As an oxygen sensitive fluorescent probe, the design of hyproxyprobe-1 is based on oxygen sensitive fluorescent dyes. In hypoxic environment, nitroimidazole in the hyproxyprobe-1 reduced by the nitroreductase in the cell to emit green fluorescence, and the fluorescence intensity deepens with the increase of the degree of hypoxia. Large areas of green fluorescence represented for hypoxia was remarked in the PBS + Laser and Free ICG + Laser treated group (Fig. 2E). The hypoxia status of the tumor in the RINA + Laser treated group was slightly relieved, which may be due to that sufficient hyperthermia accelerated blood flow and increased intravascular O_2 concentration in tumor tissues [1, 52]. Especially there was very little green fluorescence in RIMNA + Laser group, suggesting that MnO_2 catalyzed the generation of O_2 and relieved the hypoxia of tumor tissues. As shown in Fig. 2F, there was no visible green fluorescence indicated ROS in the PBS + Laser treated group, demonstrating that 808 nm laser irradiation alone couldn't generate ROS. The green fluorescence in Free ICG + Laser group and RINA + Laser group was faint, while that in the RIMNA + Laser group was strong, indicating that MnO_2-mediated tumor hypoxia amelioration significantly reinforced PDT effect. Tumor apoptosis *via* PTT-PDT was detected through H&E staining methods. The most necrosis tumor cells could be observed in RIMNA + Laser group, implying the enhanced PTT-PDT combined effect promoted tumor apoptosis (Fig. 2G). Besides, H&E images demonstrated that there was no obvious histopathological damage of major organ tissues (Supporting Information Fig. S3), proving the good biocompatibility of RIMNA.

Immune responses in vivo

DCs play a key role in the initiation and moderation of innate and adaptive immunities [53, 54]. To test whether RIMNA plus NIR irradiation could induce DCs maturation for initial immune response in vivo, tumor-draining lymph nodes were removed and stained. The results demonstrated that the expression levels of CD40, CD80, and CD86 on the surface of DCs were notably reinforced in the groups treated by RIMNA + Laser compared with other groups (Fig. 3A-F). RIMNA-based photoimmunotherapy could induce the largest amount of TAAs production, combined with the immunostimulatory effect of MPLA, promoting the highest maturation and stimulation level of DCs.

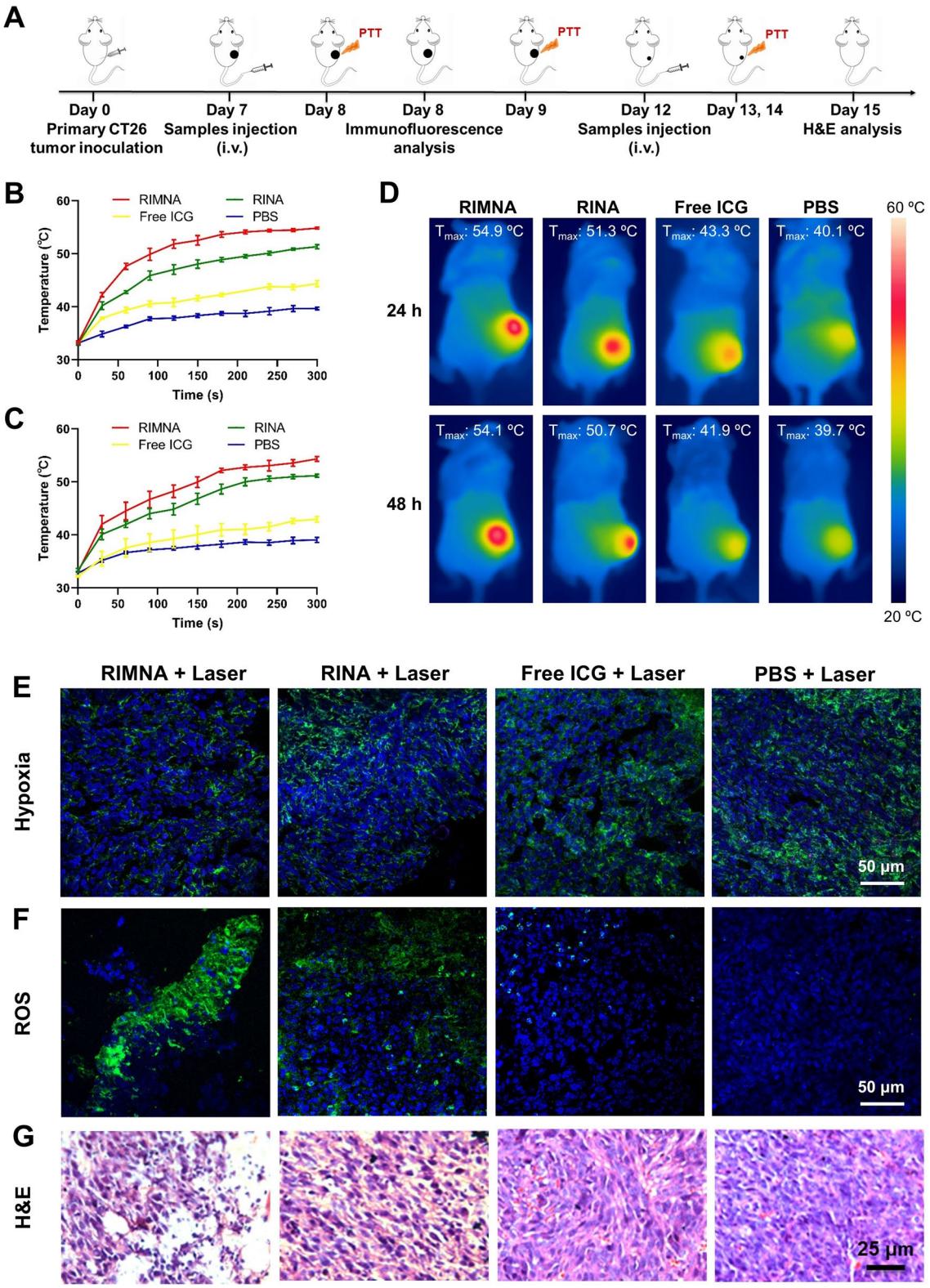

Fig. 2 PTT-PDT effect in vivo. (**A**) Schematic diagram of the treatment plan. The temperature change curves of tumor sites at (**B**) 24 h or (**C**) 48 h timepoint after administration ($n = 3$). (**D**) Representative NIR thermography at 24–48 h timepoint. CLSM images of (**E**) hypoxia and (**F**) ROS generation in tumor site after indicated treatments (Scale bar = 50 μm). (**G**) H&E images of the tumors (Scale bar = 25 μm)

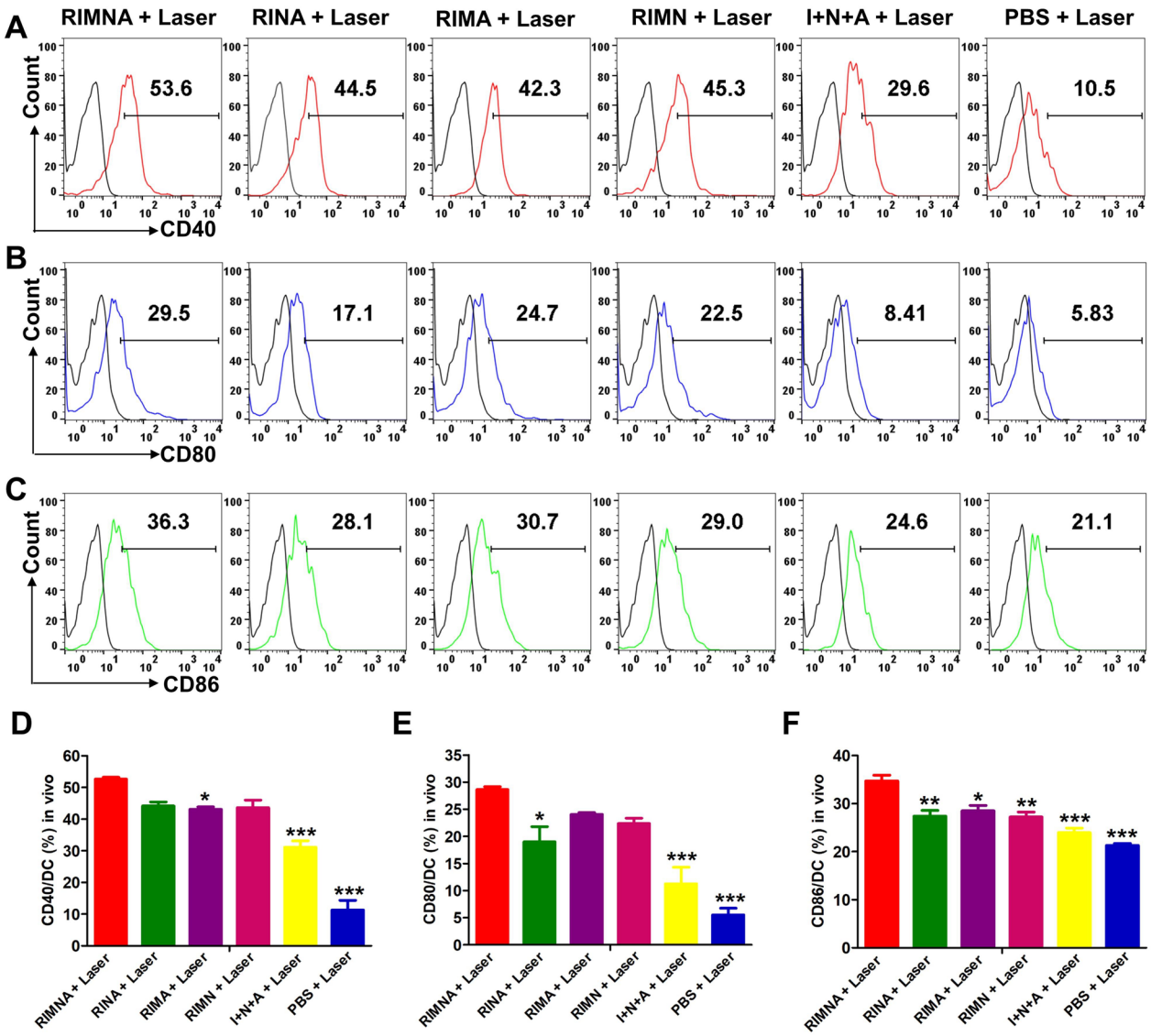

Fig. 3 DCs activation in tumor-draining lymph nodes. Representative flow cytometric plots of (**A**) CD40, (**B**) CD80, and (**C**) CD86 expression on the membrane of DCs from the lymph nodes of CT26 tumor-bearing mice following indicated treatments. Corresponding quantification of (**D**) CD40, (**E**) CD80, and (**F**) CD86 ($n = 3$). Data were displayed as mean ± SEM (*$P < 0.05$, **$P < 0.01$, ***$P < 0.001$ vs. RIMNA + Laser group)

We further estimated the effect of RIMNA + Laser on tumor immune microenvironment and systemic immune activation by detecting cytotoxic T lymphocytes (CTLs) and T helper cells (Ths) in tumor and spleen. CTLs ($CD3^+CD8^+$) and Ths ($CD3^+CD4^+$) are vital parts of the adaptive immunity, which kill tumor cells directly or activate the immune cells [55]. As shown in Fig. 4A and B, RIMNA + Laser treatment enhanced the intratumoral infiltration of CTLs and Ths, which resulted in a pronounced increase of $CD3^+CD8^+$ and $CD3^+CD4^+$ T cells to 18.4% and 11.3%, respectively. These results were supposed to be that MnO_2 loaded in RIMNA alleviated hypoxic status in tumor and reprogrammed the immunosuppressive environment, together with RIMNA polymeric micelles-mediated phototherapy, achieved potent antitumor responses. A similar increase of $CD3^+CD8^+$ and $CD3^+CD4^+$ T cells was also noted in the spleen, where RIMNA + Laser promoted them by 2.25-fold and 1.66-fold compared to PBS + Laser, respectively (Fig. 4C and D), revealing that RIMNA + Laser treatment could stimulate a systemic immune response. These results demonstrated that RIMNA + Laser effectively triggered DCs maturation in vivo to activate a powerful antitumor immune response.

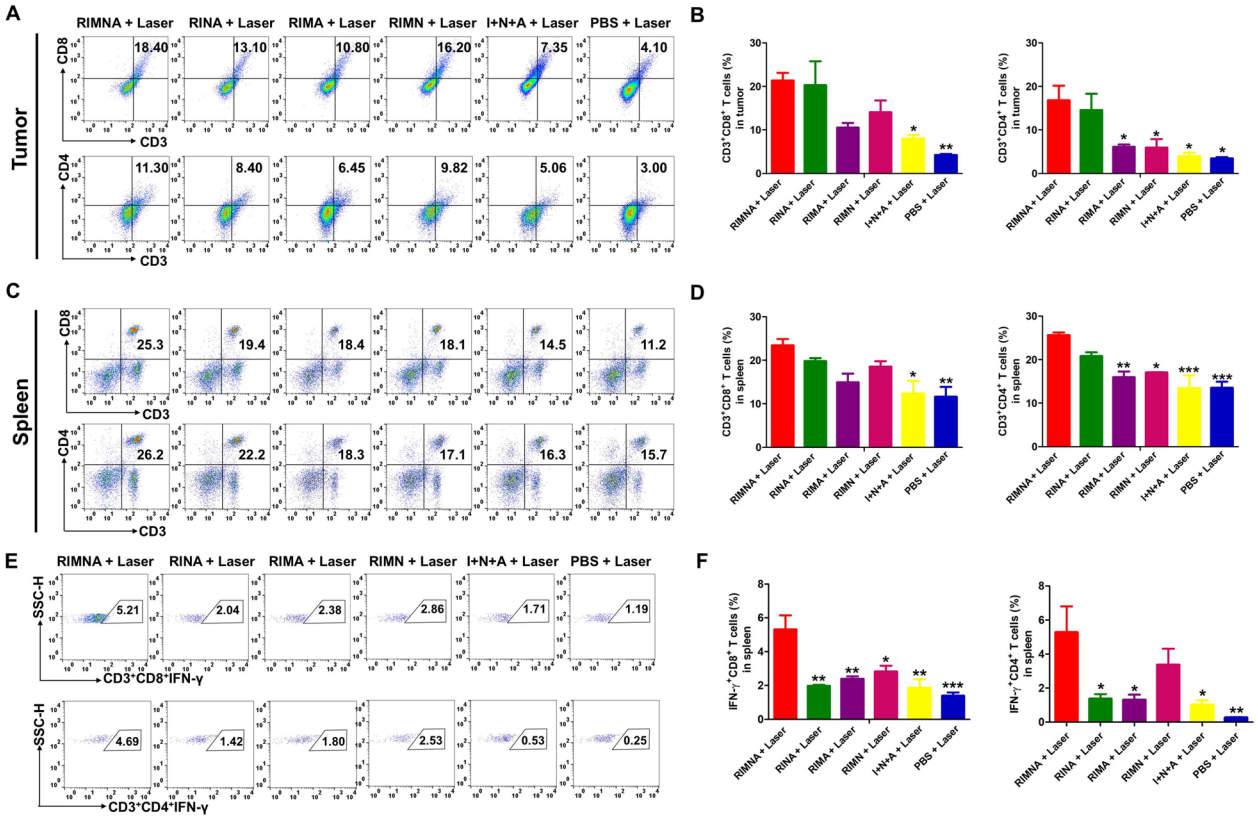

Fig. 4 Evaluation of systemic antitumor immune. (**A**, **B**) The percentages of CTLs and Ths in the tumors through flow cytometric examination ($n = 3$). (**C**, **D**) The percentages of CTLs and Ths in the spleens through flow cytometric examination ($n = 3$). (**E**, **F**) The percentages of IFN-γ-secreting $CD3^+CD8^+$ T cells and $CD3^+CD4^+$ T cells in the spleens through flow cytometric examination. Data were displayed as mean ± SEM ($n = 3$, $^*P < 0.05$, $^{**}P < 0.01$, $^{***}P < 0.001$ vs. RIMNA + Laser group)

IFN-γ is a proinflammatory cytokine released by immune cells with the functions of inhibiting tumor cell proliferation and stimulating adaptive immunity [56]. The results suggested that the percentages of $CD8^+IFN\text{-}\gamma^+$ T cells was 5.21%, 2.04%, 2.38%, 2.86%, 1.71%, and 1.19% in RIMNA + Laser group, RINA + Laser group, RIMA + Laser group, RIMN + Laser group, I + N + A + Laser group, and PBS + Laser group, respectively (Fig. 4E and F). Compared with PBS + Laser treatment (0.25%), RIMN + Laser treatment significantly boosted $CD4^+$ T cells secreting IFN-γ by 10.12-fold (2.53%), while RIMNA + Laser achieved the same aim by an increase of 18.76-fold (4.69%), proving that MPLA as a potent and safe adjuvant is able to bind to TLR4 and form phagosomes for inducing the secretion of proinflammatory cytokines [57]. It is worth pointing out that owing to the inhibition of IDO by NLG919, a notable rise of IFN-γ-secreting $CD8^+$ and $CD4^+$ T cells was monitored in the RIMNA + Laser group compared to RIMA + Laser group.

One of the remarkable features of adaptive immunity mediated by T cells is immune memory response, which plays a crucial role in protecting organisms from the second attack of tumor [58]. To verify whether RIMNA plus laser was able to produce an immune memory effect, the collected splenocytes suspension was stained to calculate central memory T cells (T_{CM}). The results displayed that the percentage of $CD8^+T_{CM}$ in RIMNA + Laser group was 50.7% (Supporting Information Fig. S4), which was the highest among all the groups. Similarly, the percentage of $CD4^+T_{CM}$ in RIMNA + Laser group was 44.4%, which was remarkably higher than that in RINA + Laser group (34.8%), RIMA + Laser group (33.3%), RIMN + Laser group (31.4%), I + N + A + Laser group (21.5%), and PBS + Laser group (21.3%). Therefore, the above results indicated that RIMNA + Laser treatment could trigger robust immune memory effects.

Abscopal effect of RIMNA-mediated PTT-PDT synergistic immunotherapy

Encouraged by the potent immune activation results of RIMNA + Laser treatment, we further explored the antitumor effects in vivo through the bilateral CT26 tumor model by 2 cycles of intravenous injection plus 808 nm laser irradiation every 5 days and

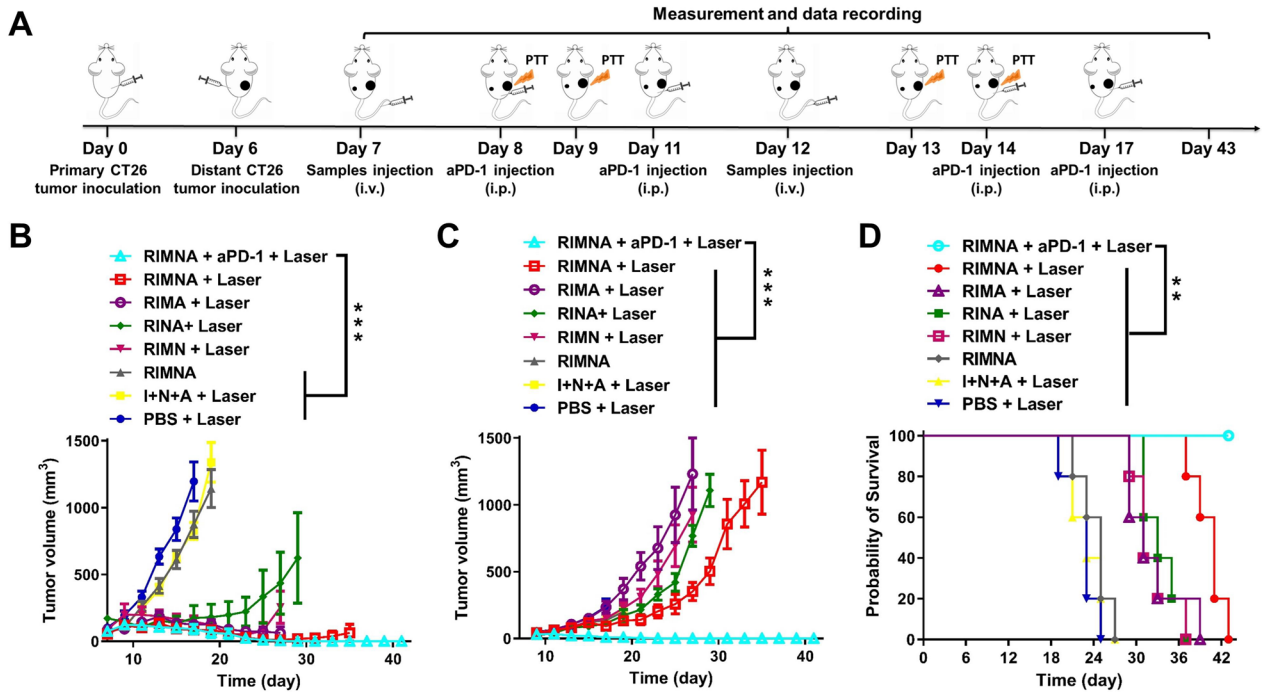

Fig. 5 Antitumor effects in vivo. (**A**) Treatment schedule in bilateral CT26 tumor model. Volume changes of (**B**) primary tumor and (**C**) distant tumor of mice after indicated treatments. (**D**) Corresponding survival curves. Data were displayed as mean ± SEM ($n = 5$, $^{**}P < 0.01$, $^{***}P < 0.001$ vs. RIMNA + aPD-1 + Laser group)

intraperitoneal administration of PD-1 antibody on days 8, 11, 14, and 17 (Fig. 5A). RINA + Laser, RIMA + Laser, and RIMN + Laser groups showed moderate tumor inhibition, while RIMNA + Laser significantly eradicated primary tumor (Fig. 5B). It's also worthy to mention that the inhibition efficacy of distant tumor in RIMNA + Laser group was much better than that of RIMA + Laser and RIMN + Laser treatment, which may be attributed to that the presence of NLG919 and MPLA evoked powerful immune response against distant tumors (Fig. 5C). Further combination of RIMNA + Laser with PD-1 antibody achieved the highest growth inhibition both of primary and distant tumors. It's worthy noted that complete tumor eradication without recurrence was achieved in all 5 tumor-bearing mice treated with RIMNA + Laser with PD-1 antibody. In contrast, although RIMNA + Laser treatment also obviously prolonged the survival time, all the mice died on day 43 (Fig. 5D). Altogether, the fact verified that RIMNA + Laser with PD-1 antibody had optimal antitumor efficacy, particularly inhibition distant tumors *via* the abscopal effect. Moreover, the above results also proved that suppressing the activity of Tregs and reactivating CTLs to block the immune escape of tumor cells has been considered a hopeful and effective antitumor strategy [28, 59].

The combination of PD-1 antibody strengthened the immune effect and antitumor metastasis

Inspired by the superior abscopal effect of RIMNA + Laser combined with PD-1 antibody, we next investigated its anti-metastasis mechanism and efficacy. The RIMNA + aPD-1 + Laser group increased the proportions of CTLs and Ths by 2.38- and 2.30-fold compared to PBS + Laser group, respectively (Fig. 6A and B, Supporting Information Fig. S5A and B). It's worthy noted that higher activation level of CTLs and Ths were observed in the spleens following treatment with RIMNA + aPD-1 + Laser (Fig. 6C and D, Supporting Information Fig. S5C and D). Moreover, RIMNA + aPD-1 + Laser treatment increased the IFN-γ-secreting CTLs ratio by ~ 15.63- and ~ 1.44-fold compared with PBS + Laser and RIMNA + Laser groups, respectively (Fig. 6E and Supporting Information Fig. S5E). Tregs are a subset of T lymphocytes that inhibit the function of effector T cells, leading to tumor development and immunosuppressive TME [55, 60]. RIMNA + aPD-1 + Laser treatment apparently decreased the proportion of Tregs compared with other groups, notably by 1.40-fold compared with PBS + Laser group (Fig. 6F and Supporting Information Fig. S5F). RIMNA + Laser could significantly upregulate the amounts of TNF-α and IL-4 in the sera, and the

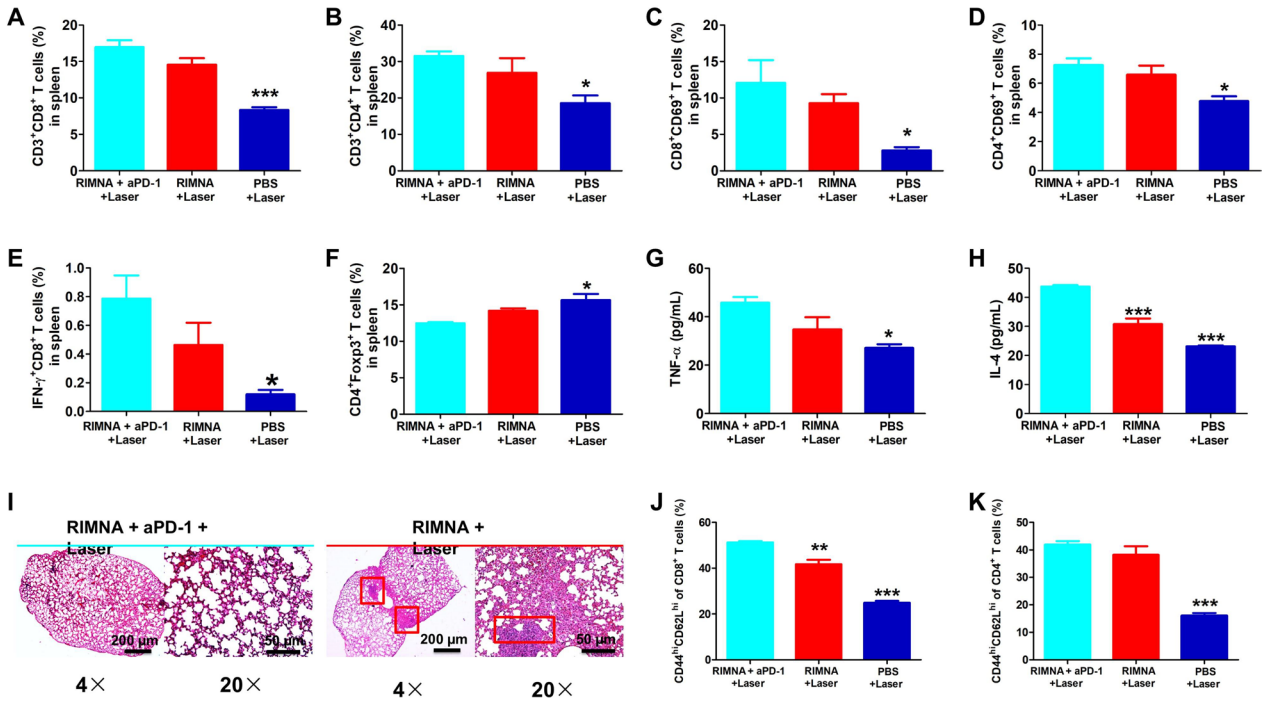

Fig. 6 Anti-metastasis effect. The percentages of (**A**) CTLs, (**B**) Ths, (**C**) $CD8^+CD69^+$ T cells, (**D**) $CD4^+CD69^+$ T cells, (**E**) IFN-γ^+CD8^+ T cells, and (**F**) Tregs in splenocytes ($n = 3$). Quantification of (**G**) TNF-α and (**H**) IL-4 released in sera after indicated treatments ($n = 3$). (**I**) H&E staining images of lung (Scale bar = 200–50 μm). The percentages of $CD44^{hi}CD62L^{hi}$ among (**J**) $CD8^+$ T cells and (**K**) $CD4^+$ T cells in spleens ($n = 3$). Data were displayed as mean ± SEM (*$P < 0.05$, **$P < 0.01$, ***$P < 0.001$ vs. RIMNA + aPD-1 + Laser group)

addition of aPD-1 further promoted these proinflammatory cytokines' secretion (Fig. 6G and H), indicating a synergistic effect to induce inflammatory response. These results suggested that RIMNA + Laser synergized with aPD-1 efficiently initiated T cell activation in vivo.

As shown in Fig. 6I, no lung nodule was observed in the RIMNA + aPD-1 + Laser group, indicating its desirable anti-metastatic effects. Furthermore, T_{CM} in spleens were quantitatively analyzed with flow cytometry. The proportions of T_{CM} among $CD8^+$ and $CD4^+$ T cells in the RIMNA + aPD-1 + Laser treated group were significantly higher than those in the PBS + Laser group ($P < 0.001$, Fig. 6J, K and Supporting Information Fig. S5G, H). Overall, those results proved that RIMNA + aPD-1 + Laser could effectively inhibit tumor growth in primary tumor, distant tumor, and pulmonary metastasis models through robust PTT-PDT synergized with immunotherapy.

Conclusions

In conclusion, we designed and developed GSH-responsive polymeric micelles RIMNA with MnO_2, NLG919, and MPLA encapsulated for augmented PTT-PDT synergized with immunotherapy. MnO_2 was able to improve ROS production *via* MnO_2-catalyzed O_2 generation in the H_2O_2-overexpressed TME, inducing strengthened PDT as well as PTT effects and the release of TAAs. Moreover, MPLA activated the TLR4 pathway to increase the secretion of proinflammatory cytokines and NLG919 inhibited IDO to reduce Tregs, thus enhancing antitumor immune response. Notably, RIMNA also attenuated TME immunosuppression by remarkably promoting the intratumoral infiltration of CTLs and Ths. Further, RIMNA-based PTT-PDT-immunotherapy exhibited excellent efficacy in suppressing the growth of distant tumor and preventing tumor metastasis of colon tumor combined with PD-1 checkpoint blockade. Taken together, this work showed the multifunctional polymeric micelles to elicit effective PTT-PDT and enlarge PTT-PDT-induced immune stimulation for steady antitumor immunity, demonstrating a prospective strategy for tumor therapy.

Supplementary Information

The online version contains supplementary material available at https://doi.org/10.1186/s12951-024-02813-w.

Supplementary Material 1: Figure S1 Inhibition of RIMNA polymeric micelles on IDO signal pathway. Data were displayed as mean ± SEM ($n = 3$, **$P < 0.01$, ***$P < 0.001$). Figure S2 Fluorescence images of CT26 tumor-bearing mice after i.v. injection of RIMNA, Free ICG or PBS. Figure S3 H&E staining images of main organs (Scale bar = 50 μm). Figure S4 The percentages of $CD44^{hi}CD62L^{hi}$ among $CD8^+$ T cells and $CD4^+$ T cells in spleens after indicated treatment. Data were expressed as mean ± SEM

($n = 3$, $^{*}P < 0.05$, $^{**}P < 0.01$, $^{***}P < 0.001$ vs. RIMNA + Laser group). Figure S5 Flow cytometric analyses of (A) $CD3^{+}CD8^{+}$ T cells, (B) $CD3^{+}CD4^{+}$ T cells, (C) $CD8^{+}CD69^{+}$ T cells, (D) $CD4^{+}CD69^{+}$ T cells, (E) IFN-$\gamma^{+}CD8^{+}$ T cells, (F) $CD4^{+}Foxp3^{+}$ T cells, (G) $CD8^{+}CD44^{hi}CD62L^{hi}$ T cells and (H) $CD4^{+}CD44^{hi}CD62L^{hi}$ T cells collected from spleens of tumor-bearing mice with different treatments.

Acknowledgements
Not applicable.

Author contributions
Chenlu Huang processed the data and wrote the manuscript. Chenlu Huang, Xinyu Yang and Huidong Li conducted the experiments. Li Zhang, Qing Guo and Qingyu Yu assisted some experiments. Hai Wang contributed to the collection of data related to flow cytometry. Linhua Zhang and Dunwan Zhu envisaged the study concept, supervised the research and edited the manuscript. All authors reviewed the manuscript.

Funding
This study was supported by National Natural Science Foundation of China (82172090, 82302390 and 82072059), CAMS Innovation Fund for Medical Sciences (2021-I2M-1-058 and 2022-I2M-2-003), China Postdoctoral Science Foundation (2022M720502), Natural Science Foundation of Tianjin Municipality (22JCQNJC00070), CAMS Union Young Scholars Support Program (2022051), and Fundamental Research Funds for the Central Universities (2019PT320028).

Data availability
No datasets were generated or analysed during the current study.

Declarations

Ethics approval and consent to participate
All animals were treated according to the regulations and guidelines of the Institute of Biomedical Engineering, Chinese Academy of Medical Science & Peking Union Medical College. Extensive efforts were made to ensure minimal suffering of the animals used during the study.

Consent for publication
All authors approved the final manuscript and the submission to this journal.

Competing interests
The authors declare no competing interests.

Author details
[1]State Key Laboratory of Advanced Medical Materials and Devices, Tianjin Key Laboratory of Biomedical Materials, Key Laboratory of Biomaterials and Nanotechnology for Cancer Immunotherapy, Institute of Biomedical Engineering, Tianjin Institutes of Health Science, Chinese Academy of Medical Sciences & Peking Union Medical College, Tianjin 300192, China. [2]Tianjin Central Hospital of Obstetrics and Gynecology, Tianjin 300100, China.

Received: 6 July 2024 Accepted: 27 August 2024
Published online: 05 September 2024

References

1. Fan W, Yung B, Huang P, Chen X. Nanotechnology for Multimodal Synergistic Cancer Therapy. Chem Rev. 2017;117:13566–638.
2. Chen J, Zhu Y, Wu C, Shi J. Nanoplatform-based Cascade Engineering for Cancer Therapy. Chem Soc Rev. 2020;49:9057–94.
3. Liu Q, Duo Y, Fu J, Qiu M, Sun Z, Adah D, Kang J, Xie Z, Fan T, Bao S, et al. Nano-immunotherapy: unique mechanisms of nanomaterials in Synergizing Cancer Immunotherapy. Nano Today. 2021;36:101023.
4. Huang C, Wang H, Yang X, Yu Q, Wang H, Zhang L, Zhao Y, Zhu D. Cascade Carrier-Free nanoparticles forming in situ nanovaccines for synergistic Photothermal-Immunotherapy of Cancer. Adv Funct Mater. 2024;34:2401489.
5. Huang C, Zhang L, Guo Q, Zuo Y, Wang N, Wang H, Kong D, Zhu D, Zhang L. Robust Nanovaccine based on polydopamine-coated mesoporous silica nanoparticles for effective Photothermal-Immunotherapy against Melanoma. Adv Funct Mater. 2021;31:2010637.
6. Xie Z, Fan T, An J, Choi W, Duo Y, Ge Y, Zhang B, Nie G, Xie N, Zheng T, Chen Y, Zhang H, Kim JS. Emerging combination strategies with phototherapy in Cancer Nanomedicine. Chem Soc Rev. 2020;49:8065–87.
7. Wang M, Song J, Zhou F, Hoover AR, Murray C, Zhou B, Wang L, Qu J, Chen WR. NIR-Triggered Phototherapy and Immunotherapy via an Antigen-capturing nanoplatform for metastatic Cancer treatment. Adv Sci (Weinh). 2019;6:1802157.
8. Liang M, Mu X, Li Y, Tan Y, Hao X, Tang Y, Wang Z, Feng W, Lu Y, Zhou X. Heptamethine Cyanine-based nanotheranostics with catalase-like activity for synergistic phototherapy of Cancer. Adv Funct Mater. 2023;33:2302112.
9. Liu X, Su H, Shi W, Liu Y, Sun Y, Ge D. Functionalized poly(pyrrole-3-carboxylic acid) nanoneedles for dual-imaging guided PDT/PTT combination therapy. Biomaterials. 2018;167:177–90.
10. Li X, Lovell JF, Yoon J, Chen X. Clinical Development and potential of Photothermal and Pphotodynamic therapies for Cancer. Nat Rev Clin Oncol. 2020;17:657–74.
11. Feng L, Zhao R, Yang L, Liu B, Dong S, Qian C, Liu J, Zhao Y. Tumor-specific NIR-Activatable nanoreactor for self-enhanced Multimodal Imaging and Cancer Phototherapy. ACS Nano. 2023;17:1622–37.
12. Huang J, Deng G, Wang S, Zhao T, Chen Q, Yang Y, Yang Y, Zhang J, Nan Y, Liu Z, Cao K, Huang Q, Ai K. A NIR-II photoactivatable ROS bomb with high-density Cu_2O-Supported MoS_2 Nanoflowers for Anticancer Therapy. Adv Sci. 2023;10:2302208.
13. Yang L, Huang B, Hu S, An Y, Sheng J, Li Y, Wang Y, Gu N. Indocyanine Green Assembled Free Oxygen-nanobubbles towards enhanced Near-infrared Induced Photodynamic Therapy. Nano Res. 2022;15:4285–93.
14. Zhou H, Liao Y, Han X, Chen DS, Hong X, Zhou K, Jiang X, Xiao Y, Shi J. ROS-Responsive nanoparticle delivery of mRNA and photosensitizer for Combinatorial Cancer Therapy. Nano Lett. 2023;23:3661–8.
15. Huang L, Zhao S, Wu J, Yu L, Singh N, Yang K, Lan M, Wang P, Kim JS. Photodynamic therapy for hypoxic tumors: advances and perspectives. Coord Chem Rev. 2021;438:213888.
16. Zhang Y, Liao Y, Tang Q, Lin J, Huang P. Biomimetic nanoemulsion for synergistic photodynamic-immunotherapy against hypoxic breast tumor. Angew Chem Int Ed. 2021;60:10647–53.
17. Gao S, Wang G, Qin Z, Wang X, Zhao G, Ma Q, Zhu L. Oxygen-generating Hybrid nanoparticles to enhance Fluorescent/photoacoustic/ultrasound imaging guided Tumor Photodynamic Therapy. Biomaterials. 2017;112:324–35.
18. Peng J, Yang Q, Li W, Tan L, Xiao Y, Chen L, Hao Y, Qian Z. Erythrocyte-membrane-coated prussian Blue/Manganese Dioxide nanoparticles as H_2O_2-Responsive oxygen generators to enhance Cancer Chemotherapy/Photothermal Therapy. ACS Appl Mater Interfaces. 2017;9:44410–22.
19. Qin Y, Huang M, Huang C, Perry HL, Zhang L, Zhu D. O_2-generating multifunctional polymeric micelles for highly efficient and selective photodynamic-photothermal therapy in Melanoma. Chin Chem Lett. 2023;35:109171.
20. You Q, Zhang K, Liu J, Liu C, Wang H, Wang M, Ye S, Gao H, Lv L, Wang C, Zhu L, Yang Y. Persistent regulation of Tumor Hypoxia Microenvironment via a Bioinspired Pt-Based Oxygen Nanogenerator for Multimodal Imaging-guided synergistic phototherapy. Adv Sci. 2020;7:1903341.
21. Zhang P, Meng J, Li Y, Yang C, Hou Y, Tang W, McHugh KJ, Jing L. Nanotechnology-enhanced Immunotherapy for Metastatic Cancer. Innov (Camb). 2021;2:100174.
22. He T, Hu M, Zhu S, Shen M, Kou X, Liang X, Li L, Li X, Zhang M, Wu Q, Gong C. A Tactical Nanomissile mobilizing Antitumor Immunity enables Neoadjuvant Chemo-Immunotherapy to Minimize Postsurgical Tumor Metastasis and Recurrence. Acta Pharm Sin B. 2023;13:804–18.
23. Galon J, Bruni D. Approaches to treat Immune Hot, altered and cold tumours with combination immunotherapies. Nat Rev Drug Discov. 2019;18:197–218.
24. Zhou Y, Liu S, Hu C, Cai L, Pang M. A covalent Organic Framework as a nanocarrier for synergistic phototherapy and immunotherapy. J Mater Chem B. 2020;8:5451–9.

25. Shen X, Zhu C, Wu Q, Shi J, Wu W, Zhao X, Sun J, Li H, Gu Z. Nanomodulators targeting tumor-resident immunosuppressive cells: mechanisms and recent updates. Nano Today. 2022;47:101641.
26. Zhang L, Wu S, Qin Y, Fan F, Zhang Z, Huang C, Ji W, Lu L, Wang C, Sun H, Leng X, Kong D, Zhu D. Targeted codelivery of an Antigen and Dual agonists by Hybrid nanoparticles for enhanced Cancer Immunotherapy. Nano Lett. 2019;19:4237–49.
27. Zhu D, Hu C, Fan F, Qin Y, Huang C, Zhang Z, Lu L, Wang H, Sun H, Leng X, Wang C, Kong D, Zhang L. Co-delivery of Antigen and dual agonists by programmed mannose-targeted Cationic lipid-hybrid polymersomes for enhanced vaccination. Biomaterials. 2019;206:25–40.
28. Huang H, Jiang C, Shen S, Liu A, Gan Y, Tong Q, Chen S, Gao Z, Du J, Cao J, Wang J. Nanoenabled reversal of IDO1-Mediated immunosuppression synergizes with immunogenic chemotherapy for Improved Cancer Therapy. Nano Lett. 2019;19:5356–65.
29. Han X, Cheng K, Xu Y, Wang Y, Min H, Zhang Y, Zhao X, Zhao R, Anderson GJ, Ren L, Nie G, Li Y. Modularly designed peptide Nanoprodrug augments Antitumor immunity of PD-L1 checkpoint blockade by Targeting Indoleamine 2,3-Dioxygenase. J Am Chem Soc. 2020;142:2490–6.
30. Peng J, Xiao Y, Li W, Yang Q, Tan L, Jia Y, Qu Y, Qian Z. Photosensitizer Micelles together with IDO inhibitor enhance Cancer Photothermal Therapy and Immunotherapy. Adv Sci (Weinh). 2018;5:1700891.
31. Zhao Z, Dong S, Liu Y, Wang J, Ba L, Zhang C, Cao X, Wu C, Yang P. Tumor Microenvironment-Activable Manganese-boosted Catalytic Immunotherapy combined with PD-1 checkpoint blockade. ACS Nano. 2022;16:20400–18.
32. Hu Y, Lin L, Guo Z, Chen J, Maruyama A, Tian H, Chen X. In situ vaccination and gene-mediated PD-L1 blockade for enhanced Tumor Immunotherapy. Chin Chem Lett. 2021;32:1770–4.
33. Hu C, Song Y, Zhang Y, He S, Liu X, Yang X, Gong T, Huang Y, Gao H. Sequential delivery of PD-1/PD-L1 blockade peptide and IDO inhibitor for Immunosuppressive Microenvironment Remodeling via an MMP-2 responsive dual-targeting Liposome. Acta Pharm Sin B. 2023;13:2176–87.
34. Panda A, Ganesan S. Genomic and immunologic correlates of indoleamine 2,3-Dioxygenase pathway expression in Cancer. Front Genet. 2021;12:706435.
35. Li X, Zhou X, Liu J, Zhang J, Feng Y, Wang F, He Y, Wan A, Filipczak N, Yalamarty SSK, Jin Y, Torchilin VP. Liposomal co-delivery of PD-L1 siRNA/Anemoside B4 for enhanced Combinational Immunotherapeutic Effect. ACS Appl Mater Interfaces. 2022;14:28439–54.
36. Liu Y-T, Sun Z-J. Turning Cold tumors into hot tumors by improving T-cell infiltration. Theranostics. 2021;11:5365–86.
37. Ma S, Tian Z, Liu L, Zhu J, Wang J, Zhao S, Zhu Y, Zhu J, Wang W, Jiang R, Qu Y, Lei J, Zhao J, Jiang T. Cold to Hot: Tumor Immunotherapy by promoting vascular normalization based on PDGFB nanocomposites. Small. 2023;20:2308638.
38. Lan X, Liang J, Wen C, Quan X, Lin H, Xu Q, Chen P, Yao G, Zhou D, Yu M. Photo-manipulated Polyunsaturated fatty acid-doped liposomal hydrogel for flexible photoimmunotherapy. Chin Chem Lett. 2023;35:108616.
39. Yang X, Huang C, Wang H, Yang K, Huang M, Zhang W, Yu Q, Wang H, Zhang L, Zhao Y, Zhu D. Multifunctional nanoparticle-loaded Injectable Alginate Hydrogels with Deep Tumor Penetration for enhanced chemo-immunotherapy of Cancer. ACS Nano. 2024;18:18604–21.
40. Li Z, Fan F, Ma J, Yin W, Zhu D, Zhang L, Wang Z. Oxygen- and bubble-generating polymersomes for Tumor-targeted and enhanced photothermal–photodynamic combination therapy. Biomater Sci. 2021;9:5841–53.
41. Liang X, Ye X, Wang C, Xing C, Miao Q, Xie Z, Chen X, Zhang X, Zhang H, Mei L. Photothermal Cancer Immunotherapy by Erythrocyte membrane-coated Black Phosphorus Formulation. J Control Release. 2019;296:150–61.
42. Wang L, Mao Z, Wu J, Cui X, Wang Y, Yang N, Ge J, Lei H, Han Z, Tang W, Guan S, Cheng L. Engineering Layered double hydroxide-based sonocatalysts for enhanced Sonodynamic-Immunotherapy. Nano Today. 2023;49:101782.
43. Ding B, Zheng P, Ma Pa, Lin J. Manganese oxide nanomaterials: synthesis, Properties, and Theranostic Applications. Adv Mater. 2020;32:1905823.
44. Qi S, Wang Y, Zhu Y, Zhang X, Wang X, Yu X, Yang K, Bai B, Feng Y, Lei J, Zhang K, Lu Z, Zhu S, Du J, Yu G. NIR-II Fluorescence Lymphatic Imaging and intraoperative Navigation based on the isolated cage Monodisperse Strategy. Nano Today. 2023;49:101795.
45. Yang L, Hou X, Zhang Y, Wang D, Liu J, Huang F, Liu J. NIR-activated self-sensitized polymeric micelles for enhanced Cancer Chemo-Photothermal Therapy. J Control Release. 2021;339:114–29.
46. Tang F, Ding A, Xu Y, Ye Y, Li L, Xie R, Huang W. Gene and Photothermal Combination Therapy: Principle, materials, and amplified anticancer intervention. Small. 2023;20:2307078.
47. Wen J, Yang K, Sun S. MnO_2-based nanosystems for Cancer Therapy. Cheml Commun. 2020;56:7065–79.
48. Wang Y, Gou M, Gong C, Wang C, Qian Z, Lin YF, Luo F. Pharmacokinetics and Disposition of Nanomedicine using biodegradable PEG/PCL polymers as drug carriers. Curr Drug Metab. 2012;13:338–53.
49. Kwon N, Jasinevicius GO, Kassab G, Ding L, Bu J, Martinelli LP, Ferreira VG, Dhaliwal A, Chan HHL, Mo Y, Bagnato VS, Kurachi C, Chen J, Zheng G, Buzza HH. Nanostructure-driven Indocyanine Green Dimerization generates Ultra-stable phototheranostics nanoparticles. Angew Chem Int Ed. 2023;62:e202305564.
50. Gao Y, Ouyang Z, Shen S, Yu H, Jia B, Wang H, Shen M, Shi X. Manganese dioxide-entrapping dendrimers co-deliver protein and Nucleotide for Magnetic Resonance Imaging-Guided Chemodynamic/Starvation/Immune Therapy of Tumors. ACS Nano. 2023;17:23889–902.
51. Gilani SJ, Ameeduzzafar, Jafar M, Shakil K, Imam SS. Nano-carriers for the treatment of tuberculosis. Recent Pat Antiinfect Drug Discov. 2017;12:95–106.
52. Dai Y, Wang B, Sun Z, Cheng J, Zhao H, Wu K, Sun P, Shen Q, Li M, Fan Q. Multifunctional theranostic liposomes loaded with a hypoxia-activated Prodrug for Cascade-activated Tumor Selective Combination Therapy. ACS Appl Mater Interfaces. 2019;11:39410–23.
53. Liu J, Zhang Y, Yang B, Jia Y, Liu RT, Ding L, Shen Z, Chen X. Synergistic glutathione depletion and STING activation to Potentiate Dendritic Cell Maturation and Cancer Vaccine Efficacy. Angew Chem Int Ed. 2024;63:e202318530.
54. Wang N, Zuo Y, Wu S, Huang C, Zhang L, Zhu D. Spatio-temporal delivery of both intra- and extracellular toll-like receptor agonists for enhancing Antigen-specific Immune responses. Acta Pharm Sin B. 2022;12:4486–500.
55. Zhou M, Liang S, Liu D, Ma K, Yun K, Yao J, Peng Y, Hai L, Zhang Q, Wang Z. Manganese-enriched zinc Peroxide Functional nanoparticles for Potentiating Cancer Immunotherapy. Nano Lett. 2023;23:10350–9.
56. Ou W, Thapa RK, Jiang L, Soe ZC, Gautam M, Chang JH, Jeong JH, Ku SK, Choi HG, Yong CS, Kim JO. Regulatory T cell-targeted hybrid nanoparticles combined with Immuno-checkpoint blockage for Cancer Immunotherapy. J Control Release. 2018;281:84–96.
57. Yu G, Jung H, Kang YY, Mok H. Comparative evaluation of cell- and serum-derived exosomes to deliver Immune stimulators to lymph nodes. Biomaterials. 2018;162:71–81.
58. Kinjyo I, Qin J, Tan SY, Wellard CJ, Mrass P, Ritchie W, Doi A, Cavanagh LL, Tomura M, Sakaue-Sawano A, Kanagawa O, Miyawaki A, Hodgkin PD, Weninger W. Real-time Tracking of Cell Cycle Progression during $CD8^+$ effector and memory T-cell differentiation. Nat Commun. 2015;6:6301.
59. Xiao Z, Su Z, Han S, Huang J, Lin L, Shuai X. Dual pH-sensitive Nanodrug blocks PD-1 Immune Checkpoint and uses T cells to deliver NF-kappaB inhibitor for Antitumor Immunotherapy. Sci Adv. 2020;6:eaay7785.
60. Farhood B, Najafi M, Mortezaee K. $CD8^+$ cytotoxic T lymphocytes in Cancer Immunotherapy: a review. J Cell Physiol. 2019;234:8509–21.

Publisher's note